ADVANCED ENERGY MATERIALS
www.advenergymat.de

Broadband Plasmonic Photocurrent Enhancement in Planar Organic Photovoltaics Embedded in a Metallic Nanocavity

*Matthew E. Sykes, Adam Barito, Jojo A. Amonoo, Peter F. Green, and Max Shtein**

A substantial broadband increase in the external quantum efficiency (EQE) of thin-film organic photovoltaic (OPV) devices using near-field coupling to surface plasmons is reported, significantly enhancing absorption at surface plasmon resonance (SPR). The devices tested consist of an archetypal boron subpthalocyanine chloride/fullerene (SubPc/C_{60}) donor/acceptor heterojunction embedded within a planar semitransparent metallic nanocavity. The absorption and EQE are modeled in detail and probed by attenuated total internal reflection spectroscopy with excellent agreement. At SPR, the EQE can be enhanced fourfold relative to normal incidence, due to simulated nine-fold enhancement in active layer absorption efficiency. The response at SPR is thickness-independent, down to a few monolayers, suggesting the ability to excite monolayer-scale junctions with an EQE of ≈6% and a 16-fold absorption enhancement over normal incidence. These results potentially impact the future design of plasmonically enhanced thin-film photovoltaics and photodetectors and enable the direct analysis of the dynamics of photocurrent production at OPV heterojunctions.

1. Introduction

In organic photovoltaics (OPVs) and photodetectors (OPDs), surface plasmon polaritons (SPPs) have been explored for their enhancement of optical fields and large scattering cross-sections, both of which can give rise to significant absorption enhancement on- and off-surface plasmon resonance (SPR).[1,2] Such SPP modes have an extremely high optical density of states, exhibit high spatial confinement due to their evanescent character, and can efficiently couple to absorbers in the near-field.[3] Due to the strong confinement of SPP modes, optical coupling at SPR provides not only an effective means for improving absorption but also the ability to transduce optical signals in photonic circuits.[4–6] Typically, plasmonic OPVs and OPDs employ metal nanoparticles[7,8] or nanostructured electrodes[9,10] exhibiting localized surface plasmon resonance (LSPR) to improve active layer absorption. While enabling optical field enhancements, however, the inclusion of metallic nanostructures can produce unintended consequences such as free carrier trapping, exciton quenching, and morphological changes, which limit the overall performance enhancement.[11–14] Thus, while absorption can easily be improved through LSPR coupling, efficient extraction of the additional generated charges to photocurrent remains a challenge.

As an alternative to LSPR-supporting nanostructures, plasmon-enhanced absorption in OPVs can be accomplished using a planar metal-dielectric-metal (MDM) structure coupled to SPPs (**Figure 1**a).[3] This type of device exhibits highly tunable spectral and angular selectivity, and can be reliably modeled to deconvolute the photocurrent generation process at SPR. Unlike radiative and waveguide modes, SPPs in metal films exhibit high field concentrations and propagate purely in-plane. This evanescent character increases the optical path length from the device thickness at normal incidence (≈100 nm) to the SPP propagation length at SPR (>10 μm for Ag).[15] Thus, coupling to SPP modes can further improve absorption beyond what is possible in conventional planar device geometries.[16,17] Additionally, since the plasmon-supporting interfaces are external to the active layers, the MDM structure avoids changes to internal charge and exciton transport and active layer morphology from embedded nanostructures. Finally, the MDM geometry exhibits a small form factor and can be directly coupled to plasmonic interconnects for applications such as on-chip communications.[18] Previous work on SPP-based OPDs in a MDM geometry has demonstrated that SPP fields can be effectively coupled to the device active layers and efficiently harvested as photocurrent.[19–23] The earlier studies by Kume et al. explored the wavelength and angular dependence of SPP-enhanced photocurrent in single-layer CuPc Shottky diodes, while later work by Mapel et al. and Bora et al. on bilayer CuPc/C_{60} devices focused on the angular response at a single wavelength. However, none has evaluated the full spectroscopic and angular dispersion of SPP-based photocurrent generation in more efficient, bilayer OPVs.

Here, we explore the broadband response to plasmon-enhanced absorption in planar OPVs with a MDM geometry using an attenuated total reflection (ATR) method in the Kretschmann configuration (Figure 1a).[24] Using an archetypal junction of boron subpthalocyanine chloride (SubPc) and C_{60} fullerene (Figure 1b), our experiments demonstrate

M. E. Sykes, A. Barito, Prof. P. F. Green, Prof. M. Shtein
Department of Materials Science and Engineering
University of Michigan
Ann Arbor, MI 48109, USA
E-mail: mshtein@umich.edu
J. A. Amonoo, Prof. P. F. Green
Department of Applied Physics
University of Michigan
Ann Arbor, MI 48109, USA

DOI: 10.1002/aenm.201301937

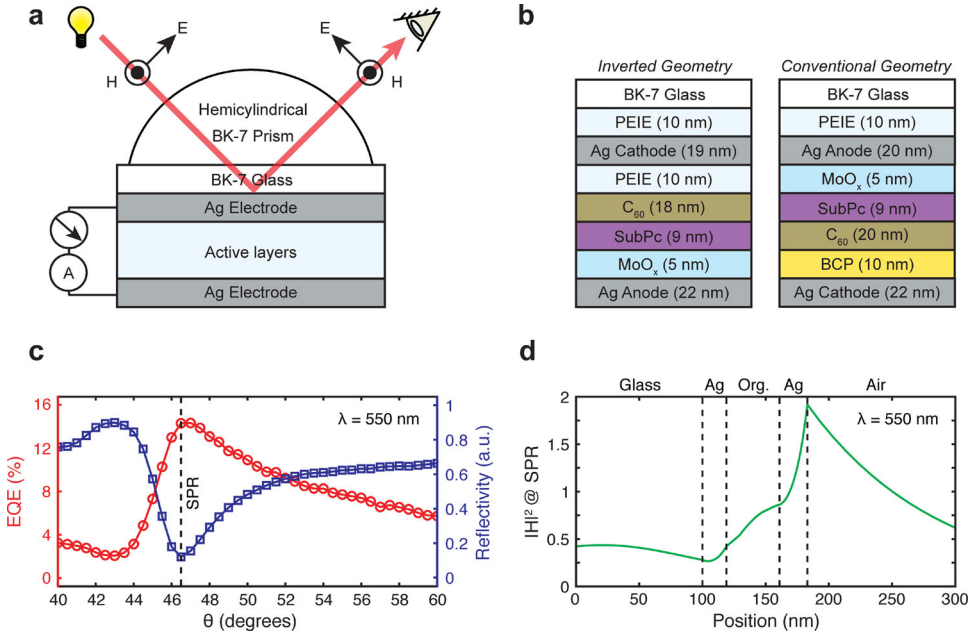

Figure 1. a) Measurement setup of MDM devices in the Kretschmann configuration using monochromatic TM-polarized light incoupled to the device via a hemicylindrical prism and index-matching fluid. For reflectivity measurements, light reflected through the prism is collected by a calibrated photodetector, while a lock-in amplifier is used to detect photocurrent generation and measure EQE. b) Device structures used in this study, displayed in the same orientation as the testing setup in (a). c) Angular scan of reflectivity and EQE at a single wavelength for the inverted device in (b), exhibiting a sharp drop in reflectivity and concomitant increase in EQE upon reaching SPR. d) Calculated H-field at the SPR condition indicated in (c), exhibiting an enhanced field magnitude and an exponential decay of the evanescent SPP mode localized at the Ag/air interface. As shown in (a), light is incident from the glass substrate in all measurements.

broadband, direct conversion of SPPs to photocurrent with an external quantum efficiency (EQE) of up to 16% and internal quantum efficiency (IQE) of ≈40%. In these devices, the EQE performance at SPR reaches 4.3× that at normal incidence. This increase is attributed to a simulated ninefold enhancement in absorption efficiency within the ultrathin active layers. In addition, we show that absorption efficiency is maximized using near-field SPR coupling in the MDM geometry and is insensitive to the active layer deposition sequence. To provide further quantitative support for these conclusions, we employ rigorous device modeling to calculate the absorption, EQE, and IQE spectra. As an extension of our results, we find that absorption efficiency in plasmonic MDM structures is relatively insensitive to active layer thicknesses down to a few monolayers, suggesting new means of probing photovoltaic energy conversion processes at the molecular-scale.

2. Results and Discussion

2.1. Device Theory and Modeling

The EQE in an OPV is determined by the product of the efficiencies for each individual step in the photocurrent generation process:

$$\eta_{EQE}(\lambda) = \eta_{Abs}(\lambda)\eta_{Diff}(\lambda)\eta_{CT}\eta_{CC} \quad (1)$$

where η_{Abs}, η_{Diff}, η_{CT}, and η_{CC} represent the active layer photon absorption, exciton diffusion, charge transfer, and charge collection efficiencies, respectively. To deconvolute absorption changes from EQE, the IQE can be defined as:

$$\eta_{IQE}(\lambda) = \frac{\eta_{EQE}(\lambda)}{\eta_{Abs}(\lambda)} \quad (2)$$

describing the efficiency by which excitons generated in the active layers are converted to photocurrent. Both η_{Abs} and η_{Diff} are wavelength-dependent since they are functions of the optical electric field in the device; spatial variation of the electric field due to near-field interference alters the local absorbed power (exciton generation profile) and hence the steady-state diffusion rate of excitons. From the product of η_{Abs} and η_{Diff} the exciton flux at the heterojunction can be calculated for a given wavelength. In contrast, η_{CT} and η_{CC} are wavelength-independent in planar heterojunction devices. η_{CT} is a function of π-orbital overlap and the kinetics of exciton transfer into bound geminate charges (polaron pairs) at the donor-acceptor heterojunction, and is typically assumed to be 100%.[25] Finally, η_{CC} is a convolution of the efficiency of polaron pair dissociation (also termed geminate charge pair separation efficiency) and the net extraction efficiency of non-geminate charges.[26] While η_{CC} is often assumed to be 100%, for many material combinations it can be considerably less than that, due to parasitic recombination processes.

The device EQE simulations used here consist of a combination of optical and drift-diffusion models. First, a transfer-matrix method was used to calculate the optical electric field profile inside of the active layers at every combination of angle and wavelength.[27] All materials were assumed to have an

isotropic refractive index taken from the literature.[27–30] While the device layers were treated as being optically coherent, the thick glass prism and substrate were treated as incoherent structures.[31] From the optical electric field profiles, the time-averaged absorbed power and exciton generation rate were determined as a function of depth in the donor/acceptor layers. Second, the exciton generation rate profile was coupled to a steady-state drift-diffusion model to determine exciton flux at the donor-acceptor heterojunction, which requires imposing a boundary condition of exciton quenching or reflection at the organic/electrode interfaces.[32] While typically it has been assumed that excitons are reflected at such interfaces, recent work has shown that the ubiquitous anode buffer layer MoO_x can quench excitons in the neighboring donor material.[33,34]

We note that exciton diffusion length (L_D) values for each active layer are often used as variable fitting parameters to account for changes in EQE spectra. However, such an approach is likely inappropriate, unless changes in L_D are accompanied by morphological or purity differences between devices. If morphology and purity remain similar among different devices being considered, it is more accurate to fix L_D and match the organic/electrode boundary conditions.[33] In this study, we assign L_D values for both the SubPc donor and C_{60} acceptor layers, 8.5 nm and 16 nm, respectively, as materials constants closely matching literature values.[35–37] This approach is more physically representitive of internal device physics and provides further insight into exciton interactions at the buried active layer interfaces. Further details on device modeling, fabrication, and testing can be found in the Supporting Information.

2.2. Device Design

Two types of devices were studied (Figure 1b): a conventional and an "inverted" layer configuration. In the conventional device structure, the anode and MoO_x layers are deposited first, followed by the donor, acceptor, exciton blocker, and cathode layers. In the "inverted" structure, the cathode is deposited onto the substrate first, followed by PEIE, the acceptor, donor, MoO_x, and anode layers. Layer thicknesses were maintained to within experimental precision between the two structures, with only the active layers' order changing relative to the SPP-supporting electrode. A similar separation distance between the silver electrodes was maintained in both geometries. In both structures, 5 nm of MoO_x was used as a work function modifying buffer layer at the anode to provide the necessary built-in potential difference for efficient charge separation at the donor-acceptor heterojunction.[38] This approach permits the selection of metal contacts for their plasmonic properties with less regard to their work functions.

Reflection and transmission spectra of devices at 7.5° and normal incidence, respectively, are shown in Figure S3 (Supporting Information). In all samples tested, we observed an excellent match between predicted and measured device optics. For these measurements, several substrates were placed in the deposition chamber and removed at incremental stages of the device fabrication process (illustrated in the insets of Figure S3, Supporting Information), yielding a sample set from the same batch. This procedure enabled fitting of layer thicknesses with nanometer precision, as slight variations between batches can have an enormous effect on the optics in MDM structures.

For accurate device modeling at SPR, it is also critical to minimize surface roughness of the electrodes. Such roughness both modifies the Fresnel coefficients at the metal/dielectric interfaces and strongly attenuates SPP propagation lengths through dissipative losses via inelastic scattering, making the response at SPR difficult to predict.[39,40] Atomic force microscopy (AFM) of the cathode and anode indicated an RMS roughness of 0.438 nm and 2.85 nm for inverted devices and 0.467 nm and 0.988 nm for conventional devices, respectively (Figure S4, Supporting Information). Smooth electrodes are made possible by the polyethylenimine ethoxylated (PEIE) wetting layer on the glass substrate, which exhibits a high affinity for silver, and results in optically-smooth films without a LSPR peak from Ag islanding (Figures S3a,d, Supporting Information). Recently PEIE has been shown to be a universal work function modifier, reducing the work function of Ag to 3.6 eV.[41] Thus we also employ it as a cathode buffer layer in the inverted device geometry.

To confirm the rectifying behavior of the OPV devices, we tested the current density–voltage dependence under simulated AM1.5 conditions (**Figure 2**). As expected for MDM devices with semitransparent electrodes, low power conversion efficiencies (PCEs) were obtained with 0.48% ± 0.04% and 0.95% ± 0.08% for inverted and conventional devices, respectively. This result is almost entirely due to low photocurrent generation; without a thick back-reflector, optical interference within the active layers is suboptimal for absorption. However, the diode behavior confirms that even with symmetric metal contacts in the MDM configuration, we are able to achieve a functioning OPV and maintain a high open-circuit voltage (0.89 ± 0.05 V to 1.05 ± 0.02 V) characteristic of SubPc-C_{60} devices.[42]

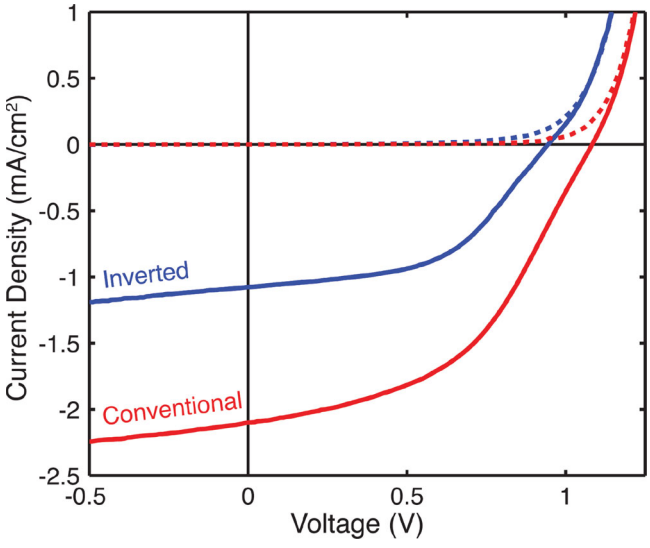

Figure 2. Current density–voltage characteristics of both inverted and conventional devices under illumination through the glass substrates with an AM 1.5 spectrum at an intensity equivalent to one sun. Testing occurred within a nitrogen-filled glove box on devices fabricated in the same batches as those measured with ATR spectroscopy.

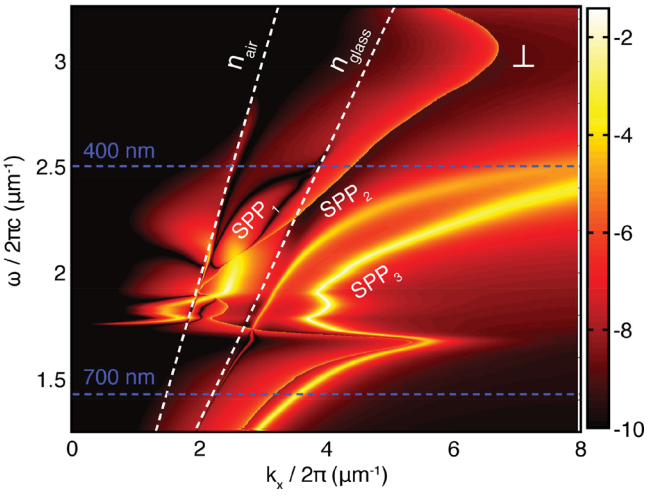

Figure 3. Calculated decay rate dispersion as a function of the in-plane wavevector (k_x) and frequency (ω) for a perpendicularly oriented exciton dipole located at the heterojunction in the inverted MDM structure. Dotted white lines indicate the light lines in air and in glass, while horizontal blue dotted lines delineate the measurement range used in this study. The dissipated power is shared among three principal decay channels: a fast mode plasmon located at the air/anode interface (SPP_1), a fast mode plasmon at the glass/cathode interface (SPP_2), and a slow plasmon mode shared between both silver contacts (SPP_3).

2.3. Surface Plasmon Resonance in "Inverted" OPV Nanocavities

Having experimentally validated our optical model at normal incidence, we now consider the spectroscopic performance of inverted devices at SPR. Figure 1c shows an ATR scan of reflectivity and EQE at a wavelength of 550 nm at angles past the critical angle for total internal reflection from the glass/silver interface. For the SPR condition, we expect a near-zero reflectivity, as the light is strongly guided in the planar device structure and back-reflection is attenuated. The drop in reflectivity is accompanied by a concomitant increase in photocurrent (EQE) upon reaching SPR. As Figure 1d shows, our simulations indicate this to be an antisymmetric SPP mode located at the air-silver interface, further confirmed by the full device dispersion curve (**Figure 3**) solved using the dyadic Green's functions.[43] The generated SPP mode in this work is characterized as a fast plasmon mode (denoted SPP_1). Additionally, there are two other SPP modes that are supported within this structure: the fast plasmon mode between the silver-substrate interface (SPP_2) and the gap plasmon mode shared between both contacts and the internal medium (SPP_3).[44] Since wavevector matching in the Kretschmann configuration is limited to below the substrate (glass) light line, it is only possible to probe SPP_1 with this method. However, in applications such as integrated optical circuits, excitation of all three modes is possible, significantly improving optical field confinement to the active layers and providing additional control over the spectroscopic dispersion.

Figure 4a,b show the modeled and experimentally measured reflectivity dispersion for an inverted device on- and off-resonance with the SPP_1 mode. We observe an excellent, quantitative match between the measured and predicted reflectivities across the visible spectrum, with the exception of an increased reflectivity at SPR ($\Delta R \approx 0.2$) near the charge transfer (CT) state absorption of C_{60} at 460 nm.[45] This is likely due to a preferential orientation of the CT exciton's transition dipole out-of-plane, which would produce an increase in the extraordinary extinction coefficient and modify the effective index of the structure at plasmon resonance. We expect this effect to be most pronounced at SPR since the electric field aligns perpendicular to the plane, exciting only perpendicularly oriented dipoles. A similar reflectivity response is observed at the sharp SubPc absorption peak (585 nm), indicating that both electronic transitions exhibit high oscillator strengths. At decreasing angles below the SPR condition, a growing proportion of the excited dipoles have an in-plane orientation, significantly reducing the effect of the anisotropic C_{60} absorption. As a result, the refractive index difference due to the observed anisotropy becomes entirely absent at normal incidence (Figure S3, Supporting Information). That being said, it does not appear that this increase in reflectivity at the 460 nm SPR peak significantly affects absorbed power in the C_{60} layer, as the higher extinction coefficient directly offsets the reduced incoupling of light into the device.[14]

Figure 4c,d show that the measured EQE response is closely matched to the model prediction across the visible spectrum. The experimentally measured angular response is slightly broadened relative to the modeled (ideal) values, which we attribute to the anode's surface roughness at the silver/air interface. To obtain these EQE fits, $\eta_{CC} = 56\%$ was assumed in the inverted device at SPR, likely limited by the polaron pair dissociation efficiency, η_{ppd}. The lower η_{ppd} is attributed to a lower built-in field in devices using symmetric contacts, compared to that in conventional indium tin oxide (ITO) based cells. Furthermore, the use of PEIE causes electron doping of adjacent fullerene thin films, which can increase geminate charge annihilation at the heterojunction and decrease η_{CC}.[46] Importantly, accurate modeling of the EQE spectra at SPR and at normal incidence for the inverted geometry can only be obtained under the assumption that the MoO_x buffer is exciton-reflecting. This assumption differs from previous demonstrations (and what we show below) of conventional SubPc/C_{60} devices employing a MoO_x buffer layer. In conventional structures, accurate modeling of EQE spectra is achieved only if exciton quenching is assumed to occur at the SubPc/MoO_x interface. To illustrate this point, **Figure 5**a compares the EQE trace at SPR to simulations assuming a reflecting or quenching boundary condition.

To understand the difference in boundary conditions at the SubPc/MoO_x interface, we draw attention to the SubPc layer thickness used in this work, 9 nm, which closely matches the L_D (8.5 nm). We conclude that the majority of exciton quenching in the inverted devices studied here are due to interface recombination and not relaxation in the bulk. Increasing the L_D cannot drastically alter the shape of the modeled EQE spectrum (Figure 5a); this can only be achieved by varying the boundary condition. We also note that if charge collection efficiency were changing between SPR and normal incidence conditions, we would see a shift in EQE across all wavelengths, not solely in the SubPc spectrum. Based on this analysis, the most appropriate conclusion is that the boundary condition at the SubPc/MoO_x interface is indeed changing from exciton quenching in conventional devices to exciton reflecting in inverted devices, based on deposition order.

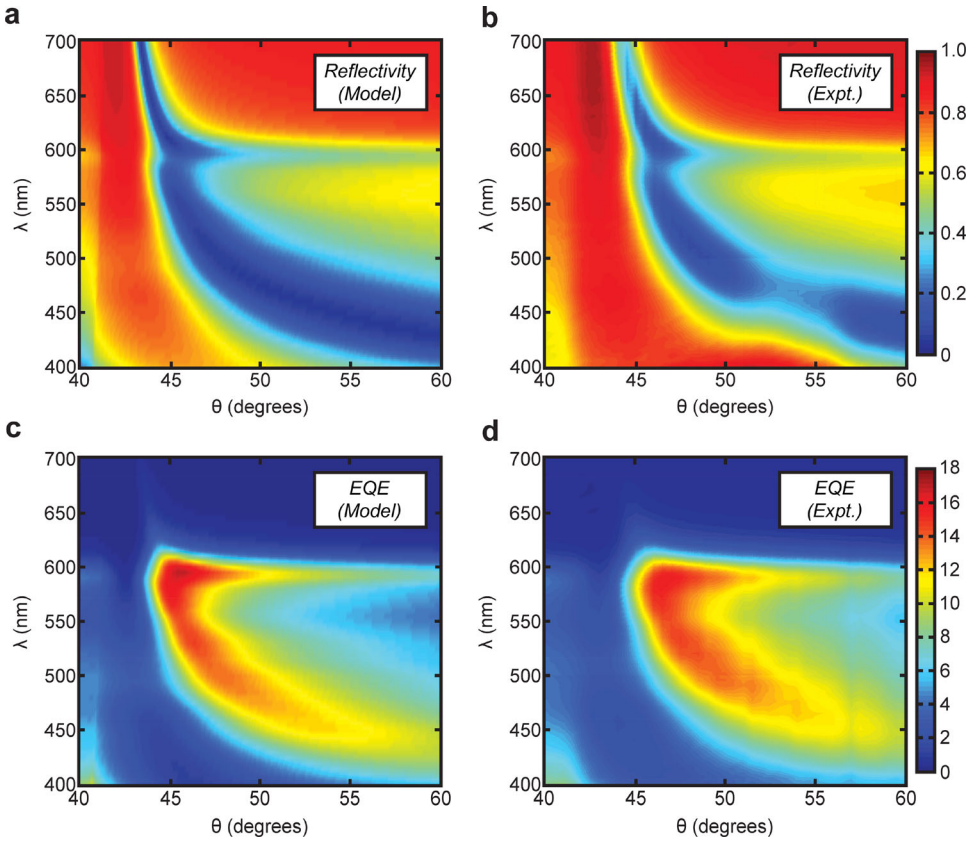

Figure 4. a) Modeled and b) measured reflectivity (a.u.) as a function of the incidence angle (in glass) and free-space wavelength for the inverted MDM device structure. The experiment accurately reproduces the shape, magnitude, and location of the guided SPP_1 mode, except for a slight increase in reflectivity at the CT-exciton absorption peak in C_{60} (λ = 460 nm). The corresponding device EQE (%) as a function of angle and wavelength is also shown for both c) modeled and d) measured values. While the reflectivity data shows a slight discrepancy in the region of C_{60} absorption, the EQE of these devices closely matches predicted values at all wavelengths. Note the same scale bars are used for both model and experiment.

It is well known that many organics in contact with MoO_x exhibit Fermi level pinning and band bending due to electron transfer to the oxide and subsequent hole buildup in the neighboring organic monolayers.[47,48] Thus it follows that exciton-polaron annihilation with this space charge is likely responsible for the observed quenching behavior by MoO_x. We hypothesize that a change in molecular orientation at the donor/MoO_x interface upon reversed deposition order could shut off this quenching pathway.

2.4. Surface Plasmon Resonance in Conventional OPV Nanocavities

As in the inverted device, the reflectivity and EQE dispersions of the SPP_1 mode of a conventional device closely match modeled values (Figure S5, Supporting Information). We observe a similar increase in reflectivity ($\Delta R \approx 0.3$) at 460 nm as seen in the inverted devices, albeit with a slightly larger deviation from the model due to an increased absorption in the C_{60} layer at SPR. Again this feature does not appear at angles close to normal incidence (Figure S3, Supporting Information), further confirming that it is due to a slight orientation anisotropy in the extinction coefficient. In contrast to the inverted devices, however, we observed a very good match to the measured EQE dispersion with the assumption that MoO_x quenches the excitons in SubPc (Figure 5d). Furthermore, we observed a ≈9% drop in η_{CC} at SPR relative to normal incidence. This reduction is a broadband effect, impacting both donor and acceptor photocurrent production, and must originate from a higher geminate charge pair recombination rate (lower polaron pair dissociation efficiency) at the heterojunction under SPR conditions.[26] Due to the low quantum yield of photon emission from geminate charge recombination in SubPc/C_{60}, it is unlikely that the increase in recombination rate at SPR is caused by optical coupling of the polaron pair emission to SPP modes. We speculate that the effect may result from hot electron injection into C_{60} from the SPP-supporting contact at resonance because the η_{CC} approaches that of the inverted geometry with electron doping from PEIE. The data cannot conclusively support such a hypothesis at this time, but warrants further investigation.

2.5. Broadband Absorption and Photocurrent Enhancement at Plasmon Resonance

Both devices exhibited a broadband enhancement in photocurrent production at SPR over what is obtained at normal

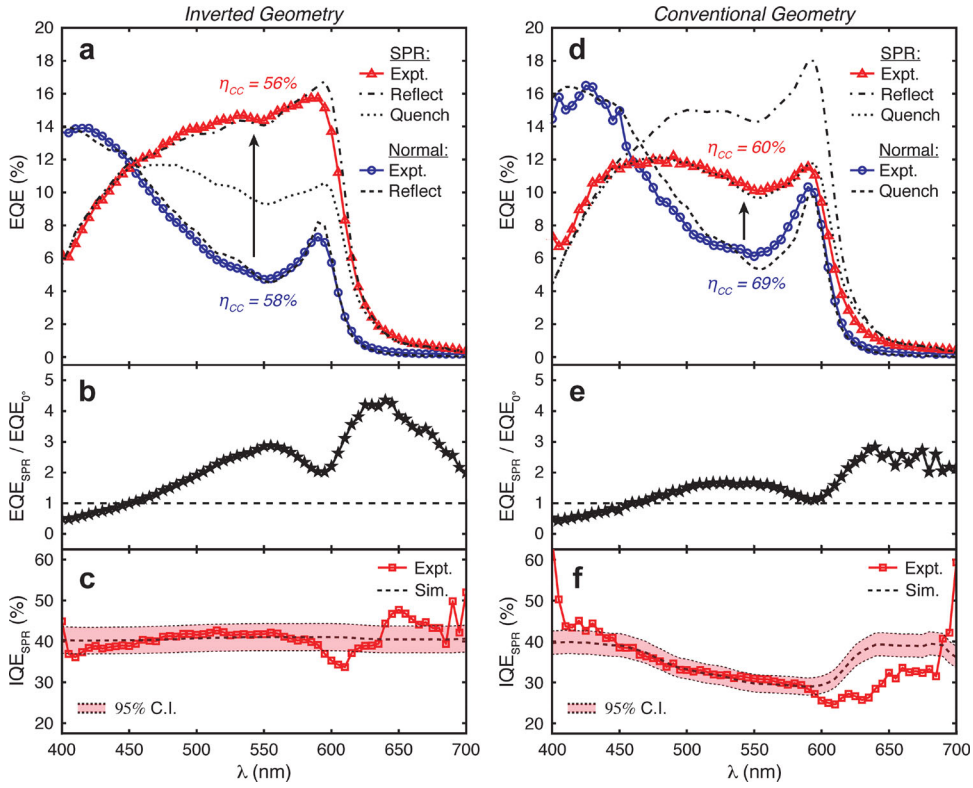

Figure 5. Spectral characteristics of a–c) an inverted device and d–f) a conventional device. a,d) Measured EQE spectra at normal incidence (blue circles) and measured along the SPR condition (red triangles) as compared to the corresponding models. The dashed lines indicate the simulated response at normal incidence for exciton reflection and quenching boundary conditions in the inverted and conventional device, respectively. The dotted and dash-dotted lines indicate the simulated response at SPR for SubPc exciton quenching and reflection boundary conditions, respectively. While collection efficiency appears to drop slightly on-resonance in (d), a significant shift in the spectral shape due to the elimination of exciton quenching in SubPc by MoO_3 is observed in (a). b,e) The corresponding measured enhancement of photocurrent and EQE at SPR over that at normal incidence. IQE at SPR in the c) inverted device and f) conventional device assuming exciton reflection and quenching at the SubPc/MoO_x interface, respectively. Red squares indicate calculated IQE values from the measured devices and dashed lines indicate the corresponding models, with shaded regions representing the 95% confidence intervals.

incidence, surpassing enhancement factors of 4.3× and 2.8× for the inverted and conventional geometries, respectively (Figure 5b,e). The measured enhancement in photocurrent is directly attributed to a non-parasitic increase in active layer absorption efficiency, reaching a factor of 9× in both geometries under SPR conditions (**Figure 6**). EQE enhancement factors were measured as slightly smaller than predicted from our calculated absorption enhancements, attributed to a low signal-to-noise ratio for both devices at normal incidence for wavelengths longer than ≈625 nm (Figure S6, Supporting Information). As shown in Figure 6a,b, the optical power is dissipated preferentially in the active layers on-resonance at wavelengths corresponding to molecular electronic transitions. At photon energies below the SubPc bandgap, most power dissipation occurs through SPP thermalization near the Ag/air interface, further confirming the nature of the SPP_1 mode probed in this study. At wavelengths shorter than ≈450 nm (approaching the Ag plasma frequency), SPP propagation is lossy, yielding a reduction in absorption efficiency and EQE below that at normal incidence (Figure 6c). Furthermore, as a result of exciton reflection at the MoO_x/SubPc interface (Figure 5c,f) in the inverted device, a 42% higher IQE in the SubPc spectrum was observed compared to the conventional device.

Interestingly, both devices exhibited nearly identical absorption spectra at SPR across the visible spectrum (Figure 6d). This is in direct contrast to performance at normal incidence, where absorption in the inverted structure is less efficient than in the conventional structure, due to a suboptimal optical field profile. Hence, the absorption and EQE enhancements at SPR are larger across the visible spectrum for the inverted device architecture. Notably, the EQE spectra at SPR exhibited a nearly 50 nm redshift in the onset of absorption (Figure 5a,d) and a nearly flat absorption profile for wavelengths ranging from 450 to 600 nm (Figure 6d). This confirms that near-field SPP coupling is suited for broadening the sharp absorption peaks in organics and improving the spectral coverage of OPVs.

Extending this study to probe the photocurrent enhancements achievable via MDM structures, we simulated the EQE of inverted devices having progressively thinner active layers down to 3 nm, the equivalent of three molecular monolayers (**Figure 7**). As expected, the IQE of the device asymptotically approached η_{CC} for thinner layers, as bulk recombination of excitons becomes negligible. Critically, the active layer absorption and EQE at the SubPc peak dropped by only 70% and 62%, respectively, for a 90% reduction in active layer thickness

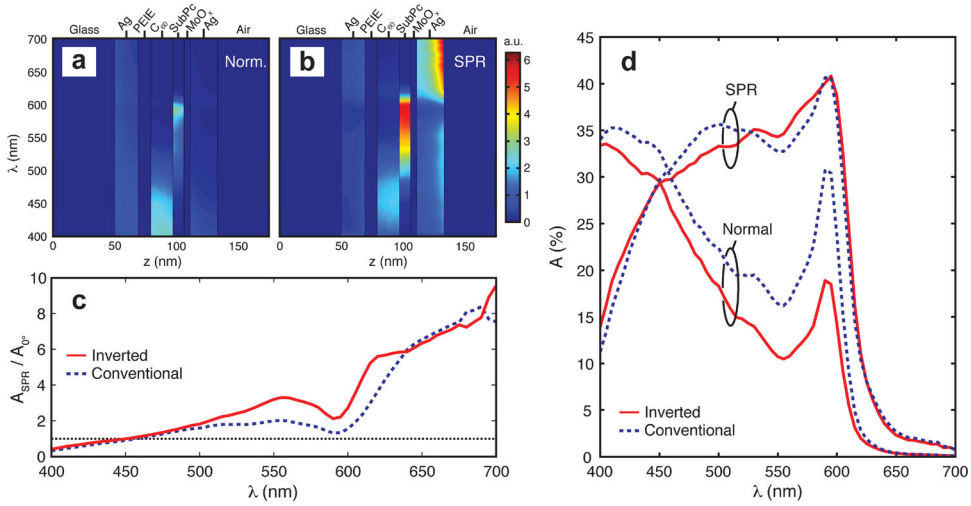

Figure 6. Spatial distribution of absorbed power vs. incident wavelength within the inverted geometry at a) normal incidence and b) SPR. c) Modeled enhancement of active layer absorptivity for both structures at SPR over that at normal incidence. d) Absorption efficiency of conventional and inverted devices simulated at normal incidence and SPR, illustrating the nearly identical absorption in both structures at SPR regardless of active layer orientation, which strongly affects absorption at normal incidence.

from the devices tested above. This corresponds to 16-fold enhancement of absorption within the active layers over that at normal incidence. Thus, SPR coupling may also offer a novel means to study molecular-scale energy harvesting and the photocurrent dynamics of organic heterojunctions, decoupled from the effects of exciton diffusion and bulk charge recombination.

3. Conclusion

We have investigated the enhancement of broadband photocurrent generation from SPP coupling in planar OPV devices with inverted and conventional MDM geometries. We observed a significantly broadened absorption with a nearly 50 nm increase in spectral coverage towards longer wavelengths and EQE enhancements at SPR reaching 4.3× and 2.8× over that at normal incidence for inverted and conventional structures, respectively. While earlier work on single-layer CuPc-based Schottky diodes having an MDM structure showed a 9× enhancement in photocurrent at SPR, those devices differ fundamentally from the heterojunctions studied here. The enhancement factors measured in this work are lower, but apply to devices with PCEs three orders of magnitude higher than the Schottky cells.[19,20] These results were quantitatively supported by device modeling, which indicated that the remarkably high EQE at SPR in the SubPc spectrum of our inverted devices arose from both a 9× enhancement in absorption efficiency and a modification of the boundary condition of the SubPc/MoO_x interface. This typically quenching interface becomes exciton-reflecting for inverted cells, indicating exciton recombination at the MoO_x boundary is sensitive to deposition order. Furthermore, the results demonstrated how SPP coupling can be used to maximize IQE, while lifting the constraint on optical incoupling effiency. Finally, these results indicated that SPR enhancement in planar metallic nanocavities enables the measurement of EQE up to 6% in a 3 nm thick active layer, representing a 16-fold enhancement in absorption efficiency.

Unlike devices incorporating embedded metallic nanoparticles or nanostructured electrodes, the devices based on planar MDM structures allow us to probe the potential of SPPs to enhance absorption and photocurrent both on- and off-resonance with the native molecular absorption peaks. Our results show that plasmonic-enhanced absorption and photocurrent is maximized at wavelengths off-resonance with the molecular absorption peaks, since efficient absorption is already achieved at normal incidence for these wavelengths. Our measurements indicate that near-field SPR coupling is an effective means for broadening not only the absorption but also photocurrent generation in OPVs and OPDs, extending their spectral coverage.

Direct means of excitation enable a number of applications, including OPDs for biosensing and refractive index monitoring (in a Kretschmann configuration), or integrated on-chip optical interconnects.[18,23] The excitation of the plasmon modes can be accomplished in other ways as well, including linear and non-linear dispersion elements and luminescent coatings.[49,50] These can potentially enable applications of our findings in photovoltaic window coatings or in lateral tandem OPV configurations.[51,52] The angle-specific requirements for enhancement of photocurrent generation are thereby relaxed, although sensitivity to polarization remains.

This work can inform and improve the rational design of plasmonic optoelectronic devices and provide further insight into the exciton quenching mechanism present at the MoO_x/organic interface. While our study has focused on the SPP_1 mode located at the Ag/air interface, coupling to other modes such as the gap plasmon (SPP_3) should minimize power dissipation in the metal contacts and further confine absorption to the active layers. Moreover, the devices in this study exhibited efficient photocurrent generation with active layer thickness on the order of $\approx\lambda/8$ at the free space wavelength of 600 nm. By reducing active layer thicknesses even more, or using low

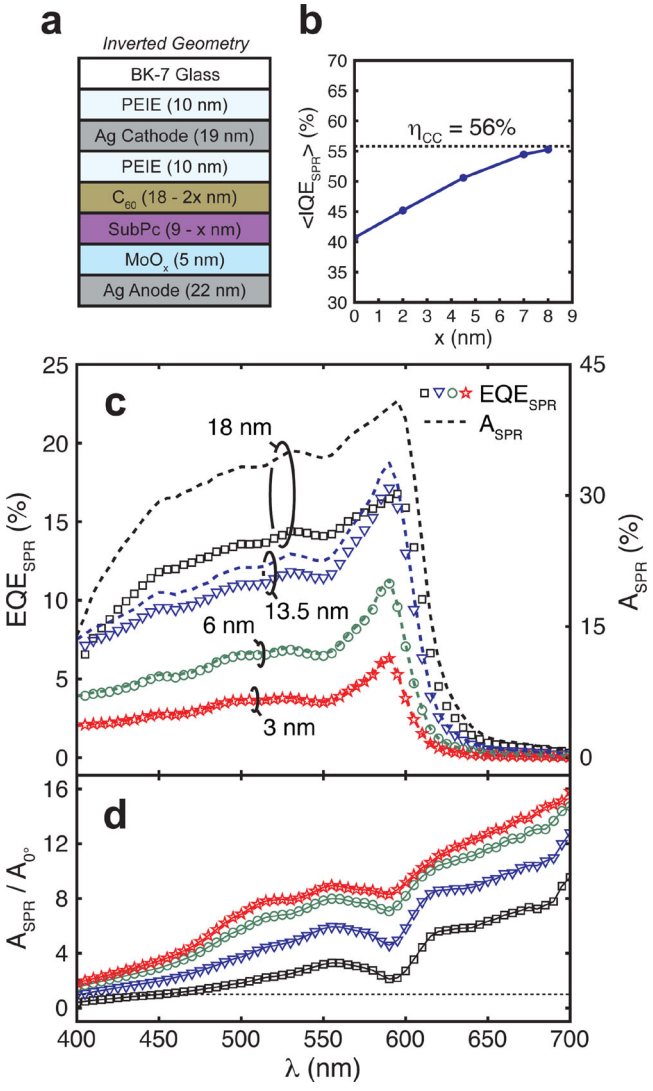

Figure 7. a) Inverted device structure with a variable reduction in active layer thickness (x), with $x = 0$ nm corresponding to the inverted devices experimentally measured in this study. b) Average IQE for the devices in (a), which asymptotically approaches η_{CC}. c) EQE (symbols) and absorption efficiency (dashed lines) at SPR for the displayed active layer thickness. d) Absorption efficiency enhancements at SPR over that at normal incidence for the corresponding devices in (c). All data displayed here correspond to modeled values.

bandgap organic dyes, such confinement can be dramatically improved. Indeed, simulations indicate the potential for monolayer-scale detectors. Finally, this work showed how an experimentally convenient device structure can be used to directly excite thin, flat donor-acceptor interfacial regions to study exciton dissociation processes decoupled from artifacts of bulk transport.

4. Experimental Section

Device Fabrication: 1 mm thick glass substrates (Fisher Sci.) were cleaned via heated (40 °C) sonication in detergent, deionized water, acetone, trichloroethylene, and isopropanol followed by boiling in isopropanol to remove any surface contaminants. A PEIE layer was then spin-cast from a 0.4 wt% solution in water and methoxyethanol at 5000 rpm for 60 s and annealed at 100 °C for 10 min to create a 10 nm thick wetting layer with a refractive index matching that of glass. For inverted devices, a 19 nm thick Ag cathode was then deposited using vacuum thermal evaporation (VTE) at a rate of 5 Å s^{-1} to ensure an optically smooth film. A second layer of PEIE was then spin cast to form a 10 nm layer on the cathode and act as a work function modifying layer. Next the small molecular acceptor and donor materials, C_{60} and SubPc, and the MoO_x buffer layer were VTE deposited with thicknesses of 18, 9, and 5 nm at deposition rates of 1, 0.5, and 0.5 Å s^{-1} respectively. Devices were shadow masked and a 22 nm Ag anode was deposited with a diameter of 1 mm at a rate of 1 Å s^{-1} to prevent shorting. For conventional device fabrication, 10 nm PEIE was spin-coated on the glass substrate followed by VTE deposition of 20 nm thick Ag anode, 5 nm MoO_x, 9 nm SubPc, 20 nm C_{60}, and 10 nm of bathocuproine (BCP) as an exciton blocking layer. Devices were then masked and a 22 nm Ag cathode was deposited. Depositions by VTE were all carried out at pressures below 5×10^{-7} Torr, with a rotating substrate held at room temperature; the entire device fabrication sequence was performed within a nitrogen-filled glove box containing less than 1 ppm O_2 and H_2O.

The organic materials SubPc (>99%), C_{60} (>99.5%), and BCP (>99%) were purchased from Luminescence Technology Corp., while MoO_3 (>99.99%) and Ag (>99.99%) were obtained from Sigma Aldrich and Kurt J. Lesker, respectively. The active layer materials SubPc and C_{60} were additionally purified once through vacuum thermal gradient sublimation.

Spectrophotometry: Transmissivity and reflectivity spectra (at normal and 7.5° incidence, respectively) were collected using a Perkin Elmer Lambda 750 UV/Vis/NIR spectrophotometer and used to confirm layer thicknesses. In both configurations, illumination was incident on the samples through the glass substrate.

Atomic Force Microscopy: AFM measurements were performed in air with an Asylum Research Systems MFP-3D standalone system in tapping mode. Surface roughness measurements were averaged over 4 μm × 4 μm areas on each sample.

OPV Device Testing and Characterization: EQE measurements were carried out in ambient using a custom ATR Kretschmann setup (detailed in Figure S1, Supporting Information). Light from a halogen source was monochromated using a Newport 130 1/8m Monochromator with a spectral full-width-half-maximum (FWHM) of 5 nm and TM-polarized using a calcite glan-thompson polarizer. The beam was then optically chopped and collimated to less than 1° divergence through a series of lenses with a beam size slightly larger than the device area (overfilling method). The photocurrent signal was detected using a Stanford Research Systems SR530 lock-in amplifier at a modulation frequency of 185 Hz and compared to a calibrated Newport silicon photodetector (Model 1931-C and 818-SL). Samples were attached to a motorized rotation stage for angular control of the incident light, coupled into each device using a hemicylindrical BK-7 lens and index matching fluid. Devices were tested at normal incidence before and after the ATR EQE scans to confirm there was no device degradation or change in spectral response. For reflectivity measurements, the specularly reflected beam off each sample was compared to the reflected beam of the same polarization from a thick (150 nm) silvered mirror as a baseline. For both reflectivity and EQE Kretschmann measurements, a 5 nm wavelength increment and an angular step size of 0.5° were used. A detailed discussion of this measurement technique and data fitting can be found in the Supporting Information.

Current density–voltage testing was performed in a glove box without exposure to air. Devices were illuminated through the glass substrate with an Oriel solar simulator (Model 91191–1000) with an AM1.5 filter and calibrated to 100 mW cm^{-2} using an NREL-certified Si reference cell (Model PVM233 KG5). Data was collected using a Hewlett-Packard scanning parameter analyzer (Model 4156B). All device areas were measured using a Carl Zeiss A.1 optical microscope and included explicitly in calculating EQE, J_{SC}, and PCE.

Supporting Information

Supporting Information is available from the Wiley Online Library or from the author.

Acknowledgements

The authors thank Kwang Hyup An for his assistance with transfer matrix and dipole decay rate modeling. This work was supported as part of the Center for Solar and Thermal Energy Conversion, an Energy Frontier Research Center funded by the U.S. Department of Energy, Office of Science, Office of Basic Energy Sciences under Award Number DE-SC0000957. A.B. thanks the NSF for partial support of this work through the National Science Foundation Graduate Student Research Fellowship under Grant No. 1256260.

Received: December 16, 2013
Revised: February 28, 2014
Published online: April 4, 2014

[1] H. A. Atwater, A. Polman, *Nat. Mater.* **2010**, *9*, 205.
[2] K. R. Catchpole, A. Polman, *Opt. Express* **2008**, *16*, 21793.
[3] D. M. Callahan, J. N. Munday, H. A. Atwater, *Nano Lett.* **2012**, *12*, 214.
[4] D. K. Gramotnev, S. I. Bozhevolnyi, *Nat. Photonics* **2010**, *4*, 83.
[5] P. Berini, *Laser Photonics Rev.* **2014**, *8*, 197.
[6] P. Neutens, P. Van Dorpe, I. De Vlaminck, L. Lagae, G. Borghs, *Nat. Photonics* **2009**, *3*, 283.
[7] D. H. Wang, K. H. Park, J. H. Seo, J. Seifter, J. H. Jeon, J. K. Kim, J. H. Park, O. O. Park, A. J. Heeger, *Adv. Energy Mater.* **2011**, *1*, 766.
[8] X. Yang, C.-C. Chueh, C.-Z. Li, H.-L. Yip, P. Yin, H. Chen, W.-C. Chen, A. K. -Y. Jen, *Adv. Energy Mater.* **2013**, *3*, 666.
[9] B. Niesen, B. P. Rand, P. Van Dorpe, D. Cheyns, L. Tong, A. Dmitriev, P. Heremans, *Adv. Energy Mater.* **2013**, *3*, 145.
[10] S. Y. Chou, W. Ding, *Opt. Express* **2013**, *21*, A60.
[11] J.-Y. Lee, P. Peumans, *Opt. Express* **2010**, *18*, 10078.
[12] H. Choi, J.-P. Lee, S-J. Ko, J.-W. Jung, H. Park, S. Yoo, O. Park, J.-R. Jeong, S. Park, J. Y. Kim, *Nano Lett.* **2013**, *13*, 2204.
[13] S. K. Kumar, N. Jouault, B. Benicewicz, T. Neely, *Macromolecules* **2013**, *46*, 3199.
[14] R. R. Grote, S. J. Brown, J. B. Driscoll, R. M. Osgood Jr., J. A. Schuller, *Opt. Express* **2013**, *21*, A847.
[15] H. Raether, *Surface Plasmons on Smooth and Rough Surfaces and on Gratings*, Vol. *111*, Springer, Berlin **1987**.
[16] E. A. Schiff, *J. Appl. Phys.* **2011**, *110*, 104501.
[17] X. Sheng, J. Hu, J. Michel, L. C. Kimerling, *Opt. Express* **2012**, *20*, A496.
[18] H. Ditlbacher, F. R. Aussenegg, J. R. Krenn, B. Lamprecht, G. Jakopic, G. Leising, *Appl. Phys. Lett.* **2006**, *89*, 161101.
[19] T. Kume, S. Hayashi, K. Yamamoto, *Jpn. J. Appl. Phys.* **1993**, *32*, 3486.
[20] T. Kume, S. Hayashi, H. Ohkuma, K. Yamamoto, *Jpn. J. Appl. Phys.* **1995**, *34*, 6448.
[21] T. Wakamatsu, K. Saito, Y. Sakakibara, H. Yokoyama, *Jpn. J. Appl. Phys.* **1995**, *34*, L1467.
[22] J. K. Mapel, M. Singh, M. A. Baldo, K. Celebi, *Appl. Phys. Lett.* **2007**, *90*, 121102.
[23] M. Bora, K. Çelebi, J. Zuniga, C. Watson, K. M. Milaninia, M. A. Baldo, *Opt. Express* **2009**, *17*, 329.
[24] E. Kretschmann, H. Raether, *Z. Naturforsch. A* **1968**, *23*, 2135.
[25] P. Peumans, A. Yakimov, S. R. Forrest, *J. Appl. Phys.* **2003**, *93*, 3693.
[26] N. C. Giebink, G. P. Wiederrecht, M. R. Wasielewski, S. R. Forrest, *Phys. Rev. B* **2010**, *82*, 155305.
[27] L. A. A. Pettersson, L. S. Roman, O. Inganäs, *J. Appl. Phys.* **1999**, *86*, 487.
[28] D. Palik, G. Ghosh, *Handbook of Optical Constants of Solids*, Academic Press, New York **1985**.
[29] H. Gommans, D. Cheyns, T. Aernouts, C. Girotto, J. Poortmans, P. Heremans, *Adv. Funct. Mater.* **2007**, *17*, 2653.
[30] Z. T. Liu, C. Y. Kwong, C. H. Cheung, A. B. Djuriši , Y. Chan, P. C. Chui, *Synth. Met.* **2005**, *150*, 159.
[31] E. Centurioni, *Appl. Opt.* **2005**, *44*, 7532.
[32] A. K. Ghosh, T. Feng, *J. Appl. Phys.* **1978**, *49*, 5982.
[33] A. Barito, M. E. Sykes, D. Bilby, J. Amonoo, Y. Jin, S. E. Morris, P. F. Green, J. Kim, M. Shtein, *J. Appl. Phys.* **2013**, *113*, 203110.
[34] X. Xiao, J. D. Zimmerman, B. E. Lassiter, K. J. Bergemann, S. R. Forrest, *Appl. Phys. Lett.* **2013**, *102*, 073302.
[35] W. A. Luhman, R. J. Holmes, *Adv. Funct. Mater.* **2011**, *21*, 764.
[36] R. R. Lunt, N. C. Giebink, A. A. Belak, J. B. Benziger, S. R. Forrest, *J. Appl. Phys.* **2009**, *105*, 053711.
[37] H. Gommans, B. Verreet, B. P. Rand, R. Muller, J. Poortmans, P. Heremans, J. Genoe, *Adv. Funct. Mater.* **2008**, *18*, 3686.
[38] V. Shrotriya, G. Li, Y. Yao, C. W. Chu, Y. Yang, *Appl. Phys. Lett.* **2006**, *88*, 073508.
[39] I. Filiński, *Phys. Stat. Sol. B* **1972**, *49*, 577.
[40] S. Zhang, L. Berguiga, J. Elezgaray, T. Roland, C. Faivre-Moskalenko, F. Argoul, *Surf. Sci.* **2007**, *601*, 5445.
[41] Y. Zhou, C. Fuentes-Hernandez, J. Shim, J. Meyer, A. J. Giordano, H. Li, P. Winget, T. Papadopoulos, H. Cheun, J. Kim, M. Fenoll, A. Dindar, W. Haske, E. Najafabadi, T. M. Khan, H. Sojoudi, S. Barlow, S. Graham, J.-L. Brédas, S. R. Marder, A. Kahn, B. Kippelen, *Science* **2012**, *336*, 327.
[42] K. L. Mutolo, E. I. Mayo, B. P. Rand, S. R. Forrest, M. E. Thompson, *J. Am. Chem. Soc.* **2006**, *128*, 8108.
[43] K. Çelebi, T. D. Heidel, M. A. Baldo, *Opt. Express* **2007**, *15*, 1762.
[44] J. B. D. Soole, H. P. Hughes, N. Apsley, *J. Appl. Phys.* **1987**, *61*, 2022.
[45] S. Kazaoui, N. Minami, Y. Tanabe, H. J. Byrne, A. Eilmes, P. Petelenz, *Phys. Rev. B* **1998**, *58*, 7689.
[46] C.-Z. Li, C.-C. Chueh, F. Ding, H.-L. Yip, P.-W. Liang, X. Li, A. K.-Y. Jen, *Adv. Mater.* **2013**, *25*, 4425.
[47] I. Irfan, A. J. Turinske, Z. Bao, Y. Gao, *Appl. Phys. Lett.* **2012**, *101*, 093305.
[48] I. Irfan, Y. Gao, *J. Photonics Energy* **2012**, *2*, 021213.
[49] T. D. Heidel, J. K. Mapel, K. Celebi, M. Singh, M. A. Baldo, *Proc. SPIE* **2007**, *6656*, 66560I.
[50] N. C. Giebink, G. P. Wiederrecht, M. R. Wasielewski, *Nat. Photonics* **2011**, *5*, 694.
[51] R. Betancur, P. Romero-Gomez, A. Martinez-Otero, X. Elias, M. Maymó, J. Martorell, *Nat. Photonics* **2013**, *7*, 995.
[52] C. Kim, J. Kim, *Opt. Express* **2008**, *16*, 19987.

